

Photographic Visualization of Weather Forecasts with Generative Adversarial Networks

Christian Sigg¹, Flavia Cavallaro², Tobias Günther³ and Martin R. Oswald^{4,5}

¹Federal Office of Meteorology and Climatology MeteoSwiss ²Comerge

³Friedrich-Alexander-Universität Erlangen-Nürnberg

⁴ETH Zürich ⁵University of Amsterdam

Abstract

Outdoor webcam images are an information-dense yet accessible visualization of past and present weather conditions, and are consulted by meteorologists and the general public alike. Weather forecasts, however, are still communicated as text, pictograms or charts. We therefore introduce a novel method that uses photographic images to also visualize future weather conditions.

This is challenging, because photographic visualizations of weather forecasts should look real, be free of obvious artifacts, and should match the predicted weather conditions. The transition from observation to forecast should be seamless, and there should be visual continuity between images for consecutive lead times. We use conditional Generative Adversarial Networks to synthesize such visualizations. The generator network, conditioned on the analysis and the forecasting state of the numerical weather prediction (NWP) model, transforms the present camera image into the future. The discriminator network judges whether a given image is the real image of the future, or whether it has been synthesized. Training the two networks against each other results in a visualization method that scores well on all four evaluation criteria.

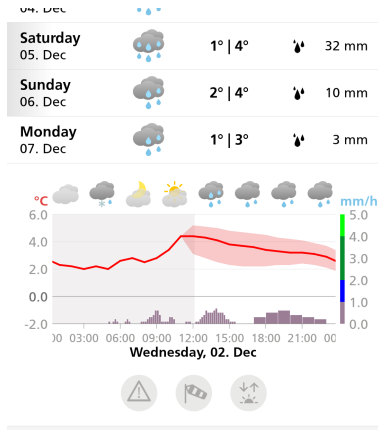
We present results for three camera sites across Switzerland that differ in climatology and terrain.

We show that users find it challenging to distinguish real from generated images, performing not much better than if they guessed randomly. The generated images match the atmospheric, ground and illumination conditions of the COSMO-1 NWP model forecast in at least 89 % of the examined cases. Nowcasting sequences of generated images achieve a seamless transition from observation to forecast and attain visual continuity.

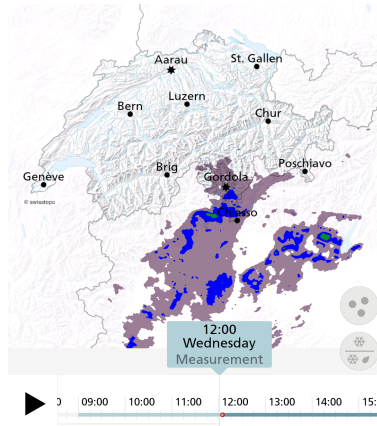
1 Introduction

Outdoor webcam images visualize past and present weather conditions, and are consulted by meteorologists and the general public alike, e.g. in aviation weather nowcasting or the planning of a leisure outdoor activity. To this purpose, MeteoSwiss currently operates 40 cameras on measurement sites of its surface network, and provides the images to the public through its web page and smartphone app (see Fig. 1c). Rega (the Swiss air rescue service) operates a similar camera network for aviation weather forecasting and flight route planning. Private companies offer cameras as a service to communities and the tourism industry, operating hundreds of outdoor web cameras all across Switzerland. However, these resources have not yet been utilized for forecasting. Instead, weather forecasts are still communicated as text, pictograms or charts (Figures 1a and 1b). We therefore introduce a novel visualization

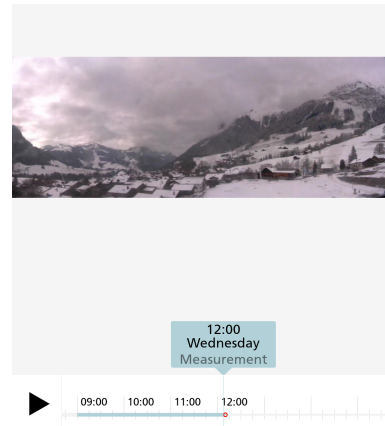
*Corresponding author: christian.sigg@meteoswiss.ch



(a) Air temperature and precipitation at a location of interest, visualized as line and bar charts. Pictograms provide additional summaries of cloud cover, sunshine and precipitation forecasts.



(b) Animation of radar maps. By pushing the time slider into the future, the visualization provides a seamless transition from measurement to forecast.



(c) Animation of past and present images taken by a web camera. We envision an analogous transition from observed to synthesized images by pushing the time slider into the future.

Figure 1: Cropped screenshots of the MeteoSwiss smartphone app, showing different ways to seamlessly combine measurements and forecasts in the same visualization.

method that uses photographic images to show future weather conditions. As with the animation of radar maps (Fig. 1b), we imagine a time slider that can be pushed beyond the present into the future (Fig. 1c) to provide a seamless transition from observation to forecast.

Photographic visualizations of weather forecasts could have numerous applications. Meteorological services could use them to communicate localized forecasts over their own webcam feeds, smartphone apps and other distribution channels. They could also provide a service to communities and tourism organizations for creating forecast visualizations that are specific for their webcam feeds.

1.1 Evaluation Criteria

Forecast visualizations must satisfy several criteria to achieve their purpose. We propose the following four to evaluate the quality of photographic visualizations of weather forecasts:

I. Realism. The images should look real and be free of obvious artifacts. Ideally, it should not be possible to tell whether a given image was taken by an actual camera, or if it was synthesized by a visualization method.

II. Matching future conditions. The images should match the future atmospheric, ground and illumination conditions in the view of the camera. However, matching every pixel of a future observed image is not possible, as the forecast does not uniquely determine the positions and shapes of clouds, for example.

III. Seamless transition. The visualization method should achieve a seamless transition from observation to forecast. It should reproduce the present image, and must retain the present weather conditions as long as they persist into the future.

IV. Visual continuity. The method should achieve visual continuity between images for consecutive lead times. For example, the movement of shadows should not show unnatural jumps across images.

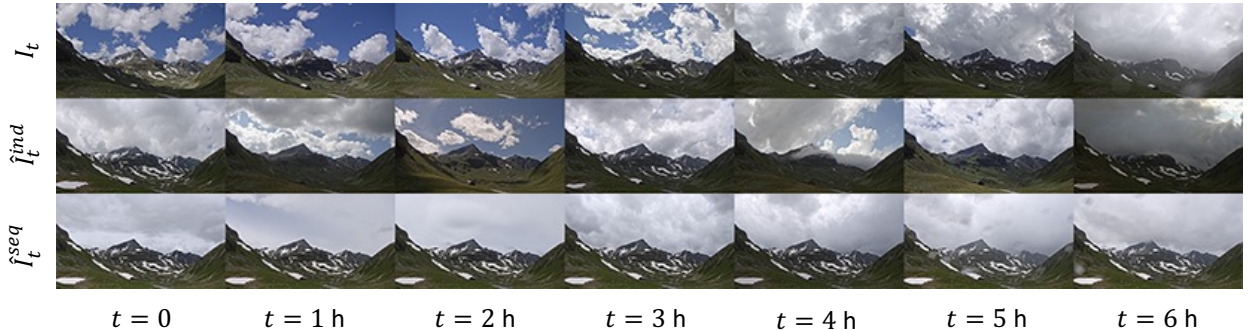


Figure 2: *Top row*: A sequence of images I_0, \dots, I_6 , taken by the Flüela camera in the Swiss Alps between 10:00 and 16:00 UTC on July 2nd, 2020. *Middle row*: A visualization created using analog retrieval of individual images from an annotated archive (see Sec. 3 for a description of the data). \hat{I}_t^{ind} is the individual image from the archive where the associated weather descriptor \hat{w}_t has the smallest Euclidean distance to the forecast w_t . *Bottom row*: A visualization created using analog retrieval of image sequences. $\hat{I}_0^{seq}, \dots, \hat{I}_6^{seq}$ is the image sequence from the archive where the associated weather descriptors $(\hat{w}_0, \dots, \hat{w}_6)$ have the smallest Euclidean distance to (w_0, \dots, w_6) .

1.2 Analog Retrieval

For a fixed camera view, such visualizations could be created using analog retrieval from an annotated image database. Given an archive of past images from the camera, annotated with the weather conditions that were present at the time the picture was taken, the forecast could be visualized by retrieving the images that most closely match the predicted conditions.

Analogs can be retrieved as individual images or whole sequences. Using *per-image* analog retrieval, \hat{I}_t^{ind} is the individual image from the archive where the associated weather descriptor \hat{w}_t has the smallest Euclidean distance to the forecast w_t for lead time t . As can be seen in the middle row of Fig. 2, using per-image analogs prioritizes matching the visible future weather conditions (our second evaluation criterion), but sacrifices the visual continuity between consecutive visualizations (our fourth criterion), with snow patches appearing and disappearing between images.

Using *sequence* analog retrieval, $\hat{I}_0^{seq}, \dots, \hat{I}_6^{seq}$ is the image sequence where the associated weather descriptors $(\hat{w}_0, \dots, \hat{w}_6)$ have the smallest Euclidean

distance to (w_0, \dots, w_6) . As can be seen in the bottom row of Fig. 2, this method satisfies the fourth criterion by construction. But to satisfy the second criterion would require that the archive contains whole sequences of images (and not just individual ones) that match the forecasted conditions.

Both methods trivially satisfy the first criterion, since the images were taken by the actual camera, but neither method achieves a seamless transition from observation to forecast (our third criterion) when I_0 shows distinctive atmospheric or ground conditions.

1.3 Image Synthesis

We therefore use image synthesis instead of image retrieval, which can be formalized as a regression problem in the following way. Given a description w_t of the future weather conditions at time t , the generator $G_0: w_t \mapsto \hat{I}_t$ synthesizes an image \hat{I}_t . This image should closely match the real future image I_t , i.e. the dissimilarity measured by a suitable loss function $L(\hat{I}_t, I_t)$ should be small. Here, $G_0(w; \theta)$ is a neural network with parameters θ , and is trained by



Figure 3: A pair of generated (*left*) and real (*right*) camera images, where G_0 was trained by minimizing the expected absolute difference of pixel values. While the ground and illumination conditions match quite well, the synthesized sky lacks detail, because it is not possible to predict the exact location and shape of the clouds from the weather forecast.

minimizing the expected loss

$$\min_{\theta} \mathbb{E}_{w_t, I_t} [L(G_0(w_t; \theta), I_t)] \quad (1)$$

over pairs (w_t, I_t) of weather forecasts and the corresponding real camera images. If the expected loss is small, then G_0 satisfies our second evaluation criterion.

The choice of L is not obvious, however. Simple regression losses, such as the mean squared difference of pixel intensities, are not suitable for our application, since it is not possible to predict the exact location and shape of clouds from the weather forecast. Thus, a pixel-by-pixel equivalence of \hat{I}_t and I_t should not be sought. In fact, using a pixel-wise loss function results in images that show a mostly uniform sky (see Figure 3), unless G_0 is trained until it overfits and reproduces examples from the training data. Instead, L should measure how well \hat{I}_t matches the overall atmospheric, ground and illumination conditions of I_t . That is, a human examiner should not be able to tell whether \hat{I}_t or I_t is the real camera image of the future, even though they are not identical.

1.4 Generative Adversarial Networks

It is unclear how to design such a loss function by hand. Goodfellow et al. [2014] introduced *Generative Adversarial Networks* (GANs) as a method for learning the loss function from training data instead.

Here, $G_1: z \mapsto \hat{I}$ synthesizes an image from a random input z , which is sampled from a suitable distribution $z \sim p(z)$, for example the Gaussian distribution. A *discriminator* $D_1: I \mapsto [0, 1]$ is introduced to mimic the human expert and to estimate the probability that the examined image I is a real image, instead of having been synthesized by the generator. $D_1(I; \eta)$ is also a neural network, with parameters η . G_1 and D_1 are trained jointly and in an adversarial fashion by optimizing the objective

$$\min_{\theta} \max_{\eta} \mathbb{E}_I [\log D_1(I; \eta)] + \mathbb{E}_z [\log \{1 - D_1(G_1(z; \theta); \eta)\}] \quad (2)$$

where $\mathbb{E}_I[\cdot]$ is the expected value w.r.t. the distribution of real images. In this min-max optimization, the generator aims to fool the discriminator, and the discriminator tries to correctly distinguish between real and generated images. The training is complete when G_1 generates images with a high degree of realism and D_1 can no longer distinguish between real and generated images, thus satisfying our first evaluation criterion.

In order to synthesize images that not only look realistic, but are also corresponding to the weather forecast at lead time t , w_t is provided as an additional input to both the generator and discriminator, $G_2(z|w_t; \theta)$ and $D_2(I|w_t; \eta)$. This *conditional* adversarial training [Mirza and Osindero, 2014] ensures that the generated images match the weather forecast and satisfy our second evaluation criterion.

Our third goal is a seamless transition from the present image I_0 to generated future images \hat{I}_t . For $t = 0$, the generator should therefore reproduce the present image, $\hat{I}_0 = I_0$. This can be achieved by extending the generator and discriminator once more. Instead of synthesizing images from a random input z , $G_3(I_0, z|w_0, w_t)$ transforms the current image I_0 into \hat{I}_t , based on the initial state w_0 and the forecast w_t of the NWP model. z adds a random component to the transformation, enabling the generator to synthesize more than one image that is consistent with the forecast when $t > 0$. The discriminator $D_3(I|I_0, w_0, w_t)$ is also conditioned on the full input. For the rest of the paper, we drop the subscripts and refer to G_3 and D_3 as G and D .

GAN-based image transformation was introduced by Isola et al. [2017]. The authors trained the networks using a linear combination of the regression objective in Eq. (1) and the adversarial objective in Eq. (2). The L_1 norm was used as the pixel-wise regression loss, and the relative importance of the regression objective was set using a tuning parameter λ . We have found that in our application, setting $\lambda > 0$ sped up the training of G for synthesizing the ground, but was detrimental for synthesizing clouds. Because their positions and shapes evolve over time, encouraging a pixel-wise consistency was again not helpful, and resulted in a sky lacking structure (as in the pure regression setting, Fig. 3). We therefore only use the adversarial objective in Eq. (2) for training the generator and discriminator.

When the atmosphere is stable on the scale of the lead time step size, there will be only small changes from I_t to I_{t+1} in the position and shape of clouds. This should be reflected in the sequence of generated images $\hat{I}_0, \hat{I}_1, \hat{I}_2, \dots$. The results in Sec. 4.4 show that the generated sequences have a good degree of temporal continuity (the fourth criterion), even though we do not explicitly model the statistical dependency between consecutive lead times t and $t + 1$. Recurrent GANs [Mogren, 2016] or adversarial transformers [Wu et al., 2020] are two potential avenues for further work in this area.

G and D can be trained for specific or arbitrary camera views. A view-independent generator could enable novel interactive applications, such as providing on-demand forecast visualizations for users equipped with a smartphone camera. But a view-independent generator will show its limits when the present view of the scenery is partially or fully blocked by opaque clouds or fog, and w_t predicts a better visibility in the future. Although G could generate natural looking scenery for the newly visible regions [Yu et al., 2018], it will not be the real scenery of this location, thus potentially confusing the user. We therefore only consider the view-dependent case in this paper, where the synthesized and real scenery match very well (see Sec. 4.2).

2 Method

Neural networks have many design degrees of freedom, such as the number of layers, the number of neurons per layer, or whether to include skip connections between layers. The choice of the loss function and the optimization algorithm are also important, especially so for training GANs. Because the generator and discriminator are trained against each other, the optimization landscape is changing with every step. Possible training failure modes are a sudden divergence of the objective (sometimes after making progress for hundreds of thousands of optimization steps), or a collapse of diversity in the generator output [Goodfellow et al., 2014]. Past research therefore has focused on finding network architectures [e.g. Radford et al., 2016], regularization [e.g. Miyato et al., 2018] and optimization schemes [e.g. Heusel et al., 2017] that increase the likelihood of training success.

We present the network architecture, weight regularization and optimization algorithm that produced the results discussed in Sec. 4. We briefly also mention alternatives that we tried, but that did not lead to consistent improvements for our application.

2.1 Network Architecture

Both G and D are encoder-decoder networks with skip connections (see Fig. 4), similar to a U-Net [Ronneberger et al., 2015]. At each stage \mathcal{E}_s of the encoder, the layer height and width is halved and the number of channels (the depth) is doubled, while the inverse is done at each decoder stage \mathcal{D}_s . By concatenating the output of \mathcal{E}_s to the output of the corresponding \mathcal{D}_s , long-range connections are introduced that skip the in-between stages.

Each encoder stage \mathcal{E}_s consists of three layers, a strided convolution (Conv) layer, followed by a batch normalization (BN) layer [Ioffe and Szegedy, 2015] and a ReLU activation layer. The decoder stages have the same layer structure, except that a transposed convolution is used in the first layer.

A full specification of the networks is provided in the companion repository. Here, we summarize the important architectural elements.

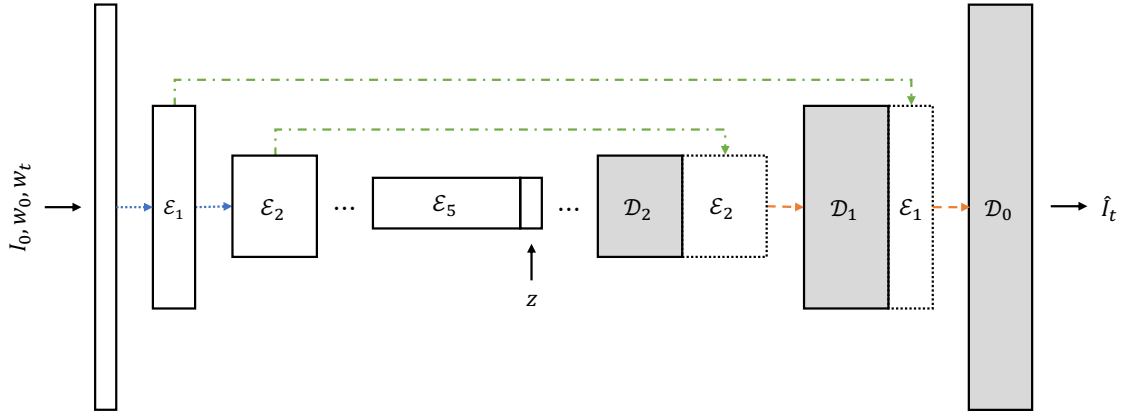


Figure 4: The encoder-decoder architecture of the generator network $G: I_0, w_0, w_t, z \mapsto \hat{I}_t$. Each encoder stage \mathcal{E}_s halves the layer height and width and doubles the depth (blue dotted arrows), while each decoder stage \mathcal{D}_s does the inverse (orange dashed arrows). The output of \mathcal{E}_s is also concatenated to the output of the corresponding \mathcal{D}_s (green dot-dashed arrows), providing additional long range connections that skip the in-between stages. A transformation of the random input $z \sim \mathcal{N}(0, 1)$ is concatenated to the output of the innermost encoder stage \mathcal{E}_5 . The complete architecture of G has additional pre- and post-processing blocks and two more stages than shown in this figure.

Generator. The input to G consists of the three color channels of I_0 and the weather descriptors. The latter are concatenated as $w = (w_0, w_t)$, and repeated and reshaped to form additional input channels, such that each channel is the constant value of an element of w . After a Conv-BN-ReLU preprocessing block, there are five encoder stages $\mathcal{E}_1, \mathcal{E}_2, \dots, \mathcal{E}_5$ that progressively halve the input height and width and double the depth, except for the last stage, where the depth is not doubled anymore to conserve GPU memory.

The random input z is sampled from a 100 dimensional Gaussian distribution with zero mean and unit variance. A dense linear layer and a reshaping layer transform z into a tensor with the same height and width as the innermost encoder stage and a depth of 128 channels.

The input to the innermost decoder stage \mathcal{D}_4 consists of the output of the last encoder stage \mathcal{E}_5 , concatenated with the transformed random input. Five decoder stages $\mathcal{D}_4, \mathcal{D}_3, \dots, \mathcal{D}_0$ restore the original height and width, followed by a Conv-BN-ReLU post-processing block and a final 1x1 convolution

with a hyperbolic tangent activation that regenerates the three color channels.

Discriminator. The input to D consists of the color channels of I_0 and I_t and the weather descriptors w_0 and w_t , which are transformed into additional input channels as in G . The encoder and decoder again have five stages each, and there is a pre-processing block before the first encoding stage and a post-processing block after the last decoding stage.

The output of the discriminator has two heads to discriminate between real and generated images on the patch and on the pixel level [Schonfeld et al., 2020]. The patch level output D_p (see Sec. 2.2) is computed by combining the output channels of the last encoder stage with a 1x1 convolution. The pixel level output D_{ij} is computed by a 1x1 convolution of the post-processing output.

We also tried alternative network architectures based on residual blocks [which add the block input to its output, see He et al., 2015], similar to the BigGAN architecture [Brock et al., 2019]. While the generator quickly learned to transform the ground, it created visible artifacts when transforming cloudy



Figure 5: An example of visible artifacts introduced by a generator architecture that is based on residual blocks. Clouds in the input image (*left*) are still partially visible in the clear sky regions of the output image (*right*), as the residual transformation learned by the generator does not fully cancel their appearance.



Figure 6: Examples of artifacts introduced by the upsampling method used in the generator. Nearest-neighbor upsampling often produced axis-aligned cloud patterns (*left*), while bilinear upsampling produced blob-like cloud shapes with a smooth boundary (*right*). Transposed convolutions avoided both problems.

skies, see Fig. 5 for an example. We conjecture that residual blocks are less suited for transformations of objects that move or evolve their shape over time, because the generator has to learn a transformation that perfectly cancels them from the block input if they are not to appear in the output.

We also tried replacing the strided convolution layers with nearest-neighbor or bilinear interpolation followed by regular convolution, which was suggested by Odena et al. [2016] to avoid checkerboard artifacts. This kind of artifact was not noticeable in the output of our final generator architecture, while nearest-neighbor upsampling often produced axis-aligned cloud patterns, and bilinear upsampling often produced overly smooth clouds, see Fig. 6.

Adding a second Conv-BN-ReLU block to each \mathcal{E}_s and \mathcal{D}_s also did not lead to a significant improvement, while doubling the number of trainable network weights.

2.2 Training Objective and Optimizer

The training objective for G and D is an extension of Eq. (2). We omit the dependency on the trainable network weights θ and η in the following equations for the sake of brevity.

The discriminator objective to be maximized consists of a sum of three components. The first two components measure how well the patch-level head D_p of the discriminator can distinguish between real

$$\mathbb{E}_{I_0, w_0, I_t, w_t} \left[\sum_p \log D_p(I_t | I_0, w_0, w_t) \right] \quad (3)$$

and generated images

$$\mathbb{E}_{I_0, w_0, w_t} \mathbb{E}_z \left[\sum_p \log [1 - D_p(G(I_0, z | w_0, w_t) | \dots)] \right] \quad (4)$$

The third component measures how well the pixel-level head D_{ij} can distinguish between the real and generated pixels of a random *cut-mix* composite C [Yun et al., 2019]

$$\mathbb{E}_C \left[\sum_{i,j} M_{ij} D_{ij}(C) + (1 - M_{ij}) \log (1 - D_{ij}(C)) \right] \quad (5)$$

The cut-mix operator combines a real and a generated image into a composite image C using a randomly generated pixel mask M , see Fig. 3 in Schonfeld et al. [2020] for an illustration, where $M_{ij} = 0$ if the pixel C_{ij} comes from the generated image, and $M_{ij} = 1$ otherwise. Cut-mixing augments the training data, and M_{ij} serves as the target label for the pixel-level head D_{ij} of the discriminator. For our application, we apply the cut-mix operator to all the input channels of the discriminator, including the channels of the weather descriptors.

The generator objective to be minimized also consists of three components. The first two components

measure how much the generator struggles to fool the discriminator on the patch level

$$\mathbb{E}_{I_0, w_0, w_t} \mathbb{E}_z \left[\sum_p \log [D_p(G(I_0, z|w_0, w_t)|\dots)] \right] \quad (6)$$

and the pixel level

$$\mathbb{E}_{I_0, w_0, w_t} \mathbb{E}_z \left[\sum_{i, j} \log [D_{ij}(G(I_0, z|w_0, w_t)|\dots)] \right] \quad (7)$$

The third component measures how similar two generated images look at the pixel level, given different random inputs $z_1, z_2 \sim \mathcal{N}(0, 1)$

$$-\lambda \cdot \mathbb{E}_{I_0, w_0, w_t} \left[\sum_{i, j, c} \left| G_{ijc}(I_0, z_1|\dots) - G_{ijc}(I_0, z_2|\dots) \right| \right] \quad (8)$$

where G_{ijc} is the intensity of channel c at pixel location (i, j) . Including this component in the objective for the generator avoids the problem of *mode collapse*, where the generator ignores z and produces a deterministic output given (I_0, w_o, w_t) . It also encourages the generator to make use of all stages of the encoder-decoder architecture, since z is injected at the innermost stage. Setting $\lambda = 1$ was sufficient to achieve both goals.

We evaluated three different optimization algorithms to train θ and η , stochastic gradient descent, RMSprop [Hinton et al., 2012] and ADAM [Kingma and Ba, 2017]. We have found that ADAM achieves the fastest loss reduction rate for our application, but that it can also produce erratic spikes in the loss curve. Spectral normalization of the training weights (see Sec. 2.3) and small learning rates were necessary to achieve a smooth training progress.

We also evaluated multiple discriminator updates per generator update, and different learning rates for the training of G and D [Heusel et al., 2017]. We found that using a two-times faster learning rate for the discriminator achieved the best results, and used 5×10^{-5} as the learning rate for the discriminator and 1×10^{-4} for the generator. The other ADAM hyperparameters were set to $\beta_1 = 0$ and $\beta_2 = 0.9$.

2.3 Spectral Normalization

GANs are difficult to train, because the optimization landscape of the adversarial training changes with every iteration. The objective can spike suddenly (after many iterations of consistent improvement), or the training can stall completely if the discriminator becomes too good at distinguishing real from generated images.

We use spectral normalization of trainable weights [Miyato et al., 2018] in all convolution layers to enforce Lipschitz continuity of the discriminator. As in Zhang et al. [2019], we found that using spectral normalization also in the generator further stabilizes the training.

3 Data

We present results for three cameras. They belong to the networks operated by MeteoSwiss and Rega, where we have access to an archive of past images. We chose sites that show a good diversity in terms of terrain and weather conditions. The camera at Cevio (e.g. Fig. 3) is located in the Maggia valley, in the southern part of Switzerland at an elevation of 421 m. The camera at Etziken (see Fig. 10) is located on the Swiss main plateau, at an elevation of 524 m. The camera at Flüela (see Fig. 7) is located on a mountain pass in the Alps, at an elevation of 2177 m.

Each camera takes pictures every 10 minutes, resulting in 144 images per day. We excluded images from our training and testing data sets that are not at all usable, such as when the camera moving head was stuck pointing to the ground, or the lens was completely covered with ice. But there was otherwise no need to clean the data set. Images were retained if there were water droplets on the lens, or if there was a minor misalignment of the camera moving head. We also did not exclude particular weather conditions such as full fog. Nevertheless, there are gaps of several days in the data series, due to camera failures that could not be fixed in a timely manner.

To limit the memory consumption and to speed up the training on the available GPU (26 GB on a single NVIDIA A100), the images were downscaled

Table 1: The weather descriptor w consists of the time of day, day of year, and the following subset of COSMO-1 output fields [see Schättler et al., 2021]:

Abbreviation	Unit	Name
ALB_RAD	%	Surface albedo for visible range, diffuse
ASOB_S	W/m ²	Net short-wave radiation flux at surface
ASWDIFD_S	W/m ²	Diffuse downward short-wave radiation at the surface
ASWDIFU_S	W/m ²	Diffuse upward short-wave radiation at the surface
ASWDIR_S	W/m ²	Direct downward short-wave radiation at the surface
ATHB_S	W/m ²	Net long-wave radiation flux at surface
CLCH	%	Cloud area fraction in high troposphere (pressure below ca. 400 hPa)
CLCM	%	Cloud area fraction in medium troposphere (between ca. 400 and 800 hPa)
CLCL	%	Cloud area fraction in low troposphere (pressure above ca. 800 hPa)
CLCT	%	Total cloud area fraction
D_TD_2M	K	2 m dew point depression
DD_10M	°	10 m wind direction
DURSUN	s	Duration of sunshine
FF_10M	m/s	10 m wind speed
GLOB	W/m ²	Downward shortwave radiation flux at surface
H_SNOW	m	Snow depth
HPBL	m	Height of the planetary boundary layer
PS	Pa	Surface pressure (not reduced)
RELHUM_2M	%	2 m relative humidity (with respect to water)
T_2M	K	2 m air temperature
TD_2M	K	2 m dew point temperature
TOT_PREC	kg/m ²	Total precipitation
TOT_RAIN	kg/m ²	Total precipitation in rain
TOT_SNOW	kg/m ²	Total precipitation in snow
U_10M	m/s	10 m grid eastward wind
V_10M	m/s	10 m grid northward wind
VMAX_10M	m/s	Maximum 10 m wind speed

from their original size to 64 by 128 pixels. Choosing powers of two for the height and width facilitates the down- and upsampling in the U-Net architecture, see Sec. 2.1. The original aspect ratios were restored using an additional horizontal resizing operation.

The weather descriptor w consists of the time of day, day of year and a subset of the hourly forecast fields provided by the COSMO-1 model (see Schättler et al. [2021] and Table 1), evaluated at the location of the camera. For the training and evaluation of the networks, we used the analysis (the initial state of the NWP model) as the optimal forecast for w_0 and also for w_t . This simplifies the evaluation of our visualization method, as it reduces the error between the NWP model state and the actual weather conditions at time t . For an operational use of the trained generator, where the analysis of the future is of course not available, one would use the current forecast for lead time t instead, without having to modify the visualization method in any other way.

w_0 and w_t can differ from the actual weather conditions visible in the camera image. The COSMO-1 fields have a limited spatial and temporal resolution of one kilometer and one hour. The camera location can thus be atypical for the NWP model grid point, and changes in weather conditions can be visible at the 10 min resolution of the camera before or after they occur in the model parameters. Using a single grid point can also be insufficient to capture the weather conditions in the view of the camera. When comparing the weather conditions visible in I_t and \hat{I}_t (see Sec. 4.2), we therefore have to distinguish between mismatches that are due to the weather descriptors (where w_0 or w_t do not accurately describe I_0 or I_t), and mismatches that are due to the generator (where \hat{I}_t does not properly visualize w_t).

We used data from the year 2019 for training, and data from the year 2020 up to the end of August (when COSMO-1 was decommissioned at MeteoSwiss) for testing. The training data sets consist of all possible tuples (w_0, w_t, I_0, I_t) , where t varies from zero to six hours. The resulting number of tuples are 712 889 for Cevio, 450 486 for Etziken and 493 096 for Flüela.

4 Results

We evaluate the forecast visualization method according to the four criteria that have been introduced in Sec. 1: how realistic the generated images look, how well they match future observed weather conditions, whether the transition from observation to forecast is seamless and whether there is visual continuity between consecutive visualizations.

Visualization methods transform data into a form that should be meaningful to humans. An evaluation of the four criteria is therefore best done using a visual inspection of the generated images. While there are objective measures for GANs that show some correlation to human judgment, such as the Fréchet Inception Distance [Heusel et al., 2017], these measures have been developed and evaluated on image data sets that are very different from ours. We therefore used objective measures only to monitor the GAN training progress, but not in the final evaluation of the generated images.

4.1 Realism

To evaluate the realism of individual generated images, we asked five coworkers at MeteoSwiss (who regularly consult the cameras of the MeteoSwiss network for their job duties, but otherwise were not involved in this project) to examine whether a presented image looks realistic or artificially generated.

The evaluation data was generated in the following way. For every camera, 75 pairs (I_0, w_0) were sampled from the test data uniformly at random, but restricted to the hours between 06:00 and 14:00 UTC to avoid too many similarly looking nighttime views. For every pair, a lead time t was sampled between 0 and 360 min (in 10 min increments), and both the real future image I_t and the generated image $\hat{I}_t = G(I_0, z|w_0, w_t)$ were added to the evaluation data set. This sampling strategy ensured that there was no overall difference in the meteorological conditions of the real and generated images, which otherwise could have influenced the examiners' accuracy.

Table 2: Results for the perceptual evaluation of real and generated images for the Cevio (left), Etziken (middle) and Flüela cameras (right). Using a browser-based data labeling tool, images were presented to five examiners with the question “What is your first impression of this image?”, and they could answer either with “looks realistic” or “looks artificially generated”. Their answers were aggregated into a confusion matrix for each camera, where the rows correspond to the ground truth, and the columns correspond to the examiners’ judgment. The overall accuracy of the examiners was 59 % for the Cevio camera, 63 % for the Etziken camera and 55 % for the Flüela camera.

Actual	Judgment		Actual	Judgment		Actual	Judgment	
	Real	Generated		Real	Generated		Real	Generated
Real	57	18	Real	52	23	Real	57	18
Generated	43	32	Generated	32	43	Generated	49	26



Figure 7: Examples of generated images that were judged to look realistic (*left*), and that contain obvious artifacts such as repeating cloud patterns (*right*).

Each examiner was then assigned 30 randomly selected images from each camera, and asked to provide their judgment on the realism of each presented image. The examiners could inspect the images at arbitrary zoom levels and look at other images in the evaluation set before giving an answer. But they were not given any background information about the images, such as the date, the lead time of the forecast or the predicted weather conditions.

The results of the evaluation are presented in Table 2. The overall low accuracy of the examiners’ judgment indicates that it was challenging for them to distinguish between real and generated images (a 50 % accuracy would correspond to random guessing). Many of the generated images look realistic enough to pass for a real image, but there were also instances where artifacts introduced by the generator were obvious at first glance (see Fig. 7 for an example).

4.2 Matching Future Conditions

To evaluate how well the forecast visualization \hat{I}_t matches the future real image I_t , we compared the atmospheric, ground and illumination conditions visible in the images. As we do not expect \hat{I}_t to match I_t in every detail (e.g. the precise shape and position of clouds do not matter), we used the following descriptive criteria to determine their overall agreement.

Atmospheric conditions. Cloud cover: *clear sky* | *few* | *cloudy* | *overcast*, cloud type: *cumuliform* | *stratiform* | *stratocumuliform* | *cirriform* and visibility: *good* | *poor*

Ground conditions. *Dry* | *wet* | *frost* | *snow*

Illumination. Time of day: *dawn* | *daylight* | *dusk* | *night*, sunlight: *diffuse* | *direct (casting shadows)*

A mismatch between the actual and visualized conditions can happen because of two different kinds of failures. The forecast descriptor w_t can fail to accurately capture the weather conditions visible in I_t , or the generated image \hat{I}_t can be inconsistent with w_t :

Inaccurate forecast. Besides COSMO-1 not being a perfect forecast model, evaluating the forecast fields only at the camera site can be insufficient to describe all of the visible weather. Furthermore, the spatial or temporal resolution of w_t can be too coarse for highly variable weather conditions. For example, the hourly granularity of the forecast can only approximately predict the time when it starts to rain.

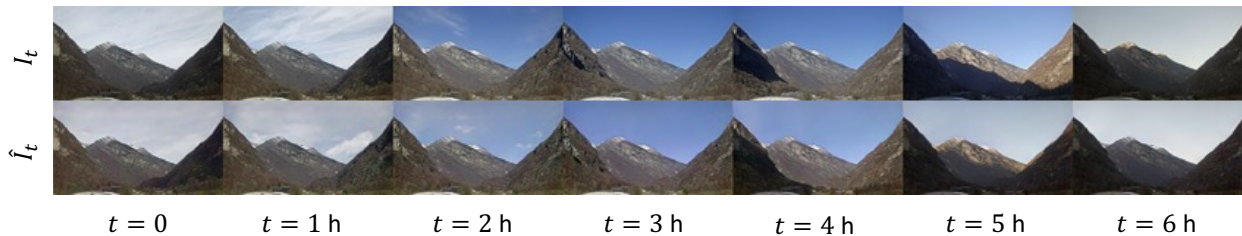


Figure 8: A sequence of images taken by the Cevio camera between 10:00 and 16:00 UTC on February 6th, 2020 (*top row*), and the corresponding images generated by $G(I_0, z|w_0, w_t)$ (*bottom row*). This visualization satisfies our four evaluation criteria. The generated images look realistic and are free of artifacts. They match the real images of the future w.r.t. atmospheric, ground and illumination conditions. The transition from observation to forecast is seamless: I_0 (*top left*) is well approximated by \hat{I}_0 (*bottom left*), and \hat{I}_1 retains the persisting weather conditions of I_0 . Finally, the progression of shadows appears natural.

Inconsistent visualization. The generator G can fail to properly account for the changes from w_0 to w_t in the transformation of I_0 to \hat{I}_t .

We used 45 pairs of the same data set as in Sec. 4.1. For each pair (I_t, \hat{I}_t) , we counted the matching descriptive criteria (at most three for the atmospheric conditions, one for the ground condition and two for the illumination conditions). If there was a mismatch in a criterion, we checked whether w_t did not accurately describe I_t (the first kind of failure), or whether \hat{I}_t was inconsistent with w_t (the second kind of failure). Only if w_t was accurate, but \hat{I}_t was inconsistent with it, did we consider the visualization to have failed.

Table 3 summarizes the results of the evaluation. In general, cloud cover and cloud type were the most difficult criteria to get right. At Cevio for example, only in 32 out of 45 cases did the cloud cover match the observed conditions. But in only 5 cases was the mismatch due to G , i.e. w_t was accurate but \hat{I}_t was inconsistent with it. The other times when there was a mismatch, w_t did not accurately describe I_t (see Fig. 9 for an example). The visualization method would therefore benefit the most from improving the accuracy of the weather forecast, e.g. by using a post-processed version of the COSMO-1 forecast with a higher spatial and temporal resolution.

Figures 8 to 11 show further examples of the range



Figure 9: The cloud amount in the generated image (*left*) is too large, compared to the observed conditions (*right*) at Cevio on April 25th 2020 at 12:00 UTC. But the mismatch is not a failure of the visualization method, as the COSMO-1 forecast predicts a 100% cloud area fraction in the medium troposphere.

of transformations that can be achieved by the generator, transforming the atmospheric and illumination conditions to match I_t , while retaining the specific ground conditions of I_0 .

4.3 Seamless Transition

For a seamless transition between observation and forecast, the generator must be able to reproduce the input image $\hat{I}_0 = I_0$ for $t = 0$. It must also retain the conditions of I_0 in $\hat{I}_1, \hat{I}_2, \dots$ as long as they persist into the future.

We evaluated the third criterion on hourly nowcasts up to six hours into the future. As can be seen in Figures 8 to 12, the generator reproduces the

Table 3: Counts of matching atmospheric, ground and illumination conditions between real and generated images I_t and \hat{I}_t at time t . For each camera, 45 random pairs (I_t, \hat{I}_t) were visually compared according to the criteria of Sec. 4.2. Whenever there was a mismatch in at least one criterion, we checked if the weather descriptors w_t of the forecast accurately describe the conditions visible in I_t . Only in this case did we count the visualization to have failed.

Camera	Matching conditions						Viz. failures
	Atmosphere			Ground	Illumination		
	Cloud cover	Cloud type	Visibility		Time of day	Diffuse/direct	
Cevio	32	35	45	45	45	40	5
Etziken	36	36	44	45	45	38	2
Flüela	31	33	26	44	41	35	5

ground and illumination conditions of I_0 very well in \hat{I}_0 . The shape and positions of clouds are reproduced closely but not exactly, giving the impression that the generator reconstructs the overall cloud pattern, but not every small detail. We could achieve pixel-level accurate reproductions of I_0 by using a residual architecture for the generator network. But as discussed in Sec. 2.1, the realism of images generated using a residual network suffered from noticeable visual artifacts for $t > 0$.

As can be seen in the bottom row of Fig. 11, the generator retains the specific conditions of I_0 (such as the position and shape of snow patches) in the visualizations $\hat{I}_1, \dots, \hat{I}_6$. This is only possible because G transforms I_0 into \hat{I}_t . As already shown in the corresponding Fig. 2, a seamless transition cannot be achieved using analog retrieval (Sec. 1.2), because an image with the specific shapes and positions of clouds and snow patches will not exist in the archive.

4.4 Visual Continuity

Finally, the consecutive visualizations \hat{I}_t, \hat{I}_{t+1} must show visual continuity, with a natural looking cloud development, change of daylight, movement of shadows, and so on. As can be seen in Figures 8 to 13, the evolution of the ground and illumination conditions matches the future observed images very closely, even though G and D do not explicitly ac-

count for the statistical dependency between t and $t + 1$. The increase or decrease in cloud cover and visibility also looks natural. By contrast, the visualizations based on individual analogs \hat{I}_t^{ind} lack continuity (Fig. 2, middle row), with snow patches appearing and disappearing, and unnatural changes in the illumination conditions.

But $G(I_0, z|w_0, w_t)$ struggled with learning image transformations that involve translations of objects across the camera view, such as the movement of the sun (Fig. 12) or of isolated clouds (Fig. 13). We conjecture that a network architecture based on Conv-BN-ReLU blocks is highly effective at transforming the appearance of objects that remain in place, but less for translations. We therefore investigated whether including non-local network layers, such as self-attention [Zhang et al., 2019], could be beneficial. But we did not achieve a consistent improvement in our experiments, neither with full nor with axis-aligned self-attention, whereas the network training time increased significantly.

The balance between visual continuity and image diversity can be tuned by changing the standard deviation σ of the random input $z \sim \mathcal{N}(0, \sigma^2)$. Increasing σ leads to a greater diversity of visualizations that are deemed consistent with the weather forecast, while decreasing σ promotes greater continuity between subsequent images (see Fig. 14). We have found that setting $\sigma = 0.5$ results in the best trade-off between the two objectives.

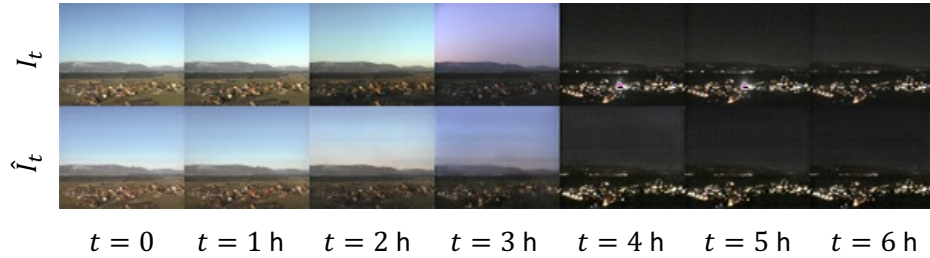


Figure 10: A sequence of images taken by the Etziken camera between 14:00 and 20:00 UTC on February 6th, 2020 (*top row*), and the corresponding images generated by $G(I_0, z|w_0, w_t)$ (*bottom row*). The generator was able to fully transform I_0 (*top left*) from daylight to nighttime conditions, including the visual appearance of illuminated street lamps and windows at $t = 4$ h.

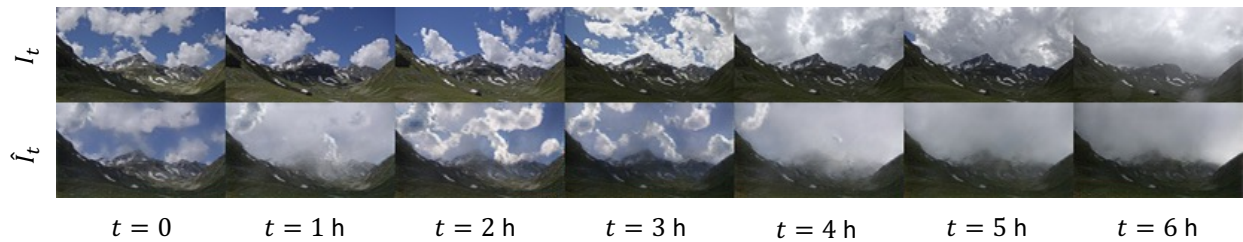


Figure 11: *Top row*: The same sequence of images as in the top row of Fig. 2, taken by the Flüela camera between 10:00 and 16:00 UTC on July 2nd, 2020. *Bottom row*: Because $\hat{I}_t = G(I_0, z|w_0, w_t)$ is a *transformation* of I_0 , the exact position and shape of snow patches are retained in $\hat{I}_1, \hat{I}_2, \dots, \hat{I}_6$.

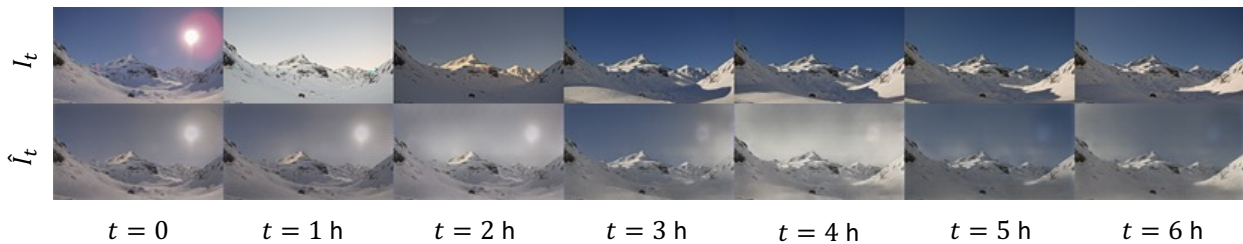


Figure 12: *Top row*: A sequence of images taken by the Flüela camera between 06:00 and 12:00 UTC on January 12th, 2020. *Bottom row*: The generator accurately transformed the illumination conditions and shadows. But it failed to learn how the sun moves across the sky. Instead of shifting the position of the sun, the sun stays in the same position and fades away gradually.

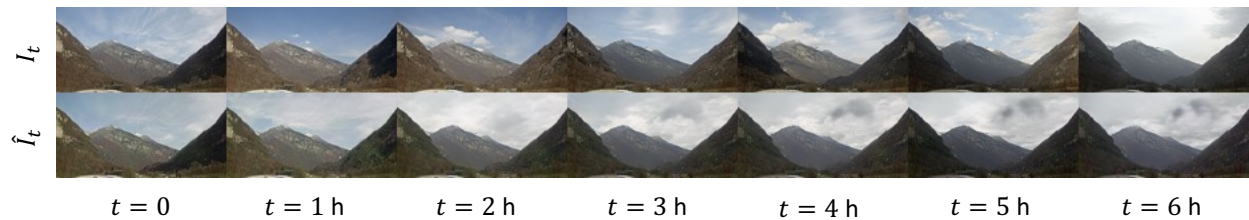


Figure 13: *Top row*: A sequence of images taken by the Cevio camera between 10:00 and 16:00 UTC on February 17th, 2020. *Bottom row*: The generated images accurately match the ground and illumination conditions, and the development of cloud shapes appears natural. But the *positions* of individual clouds remain too static over time.

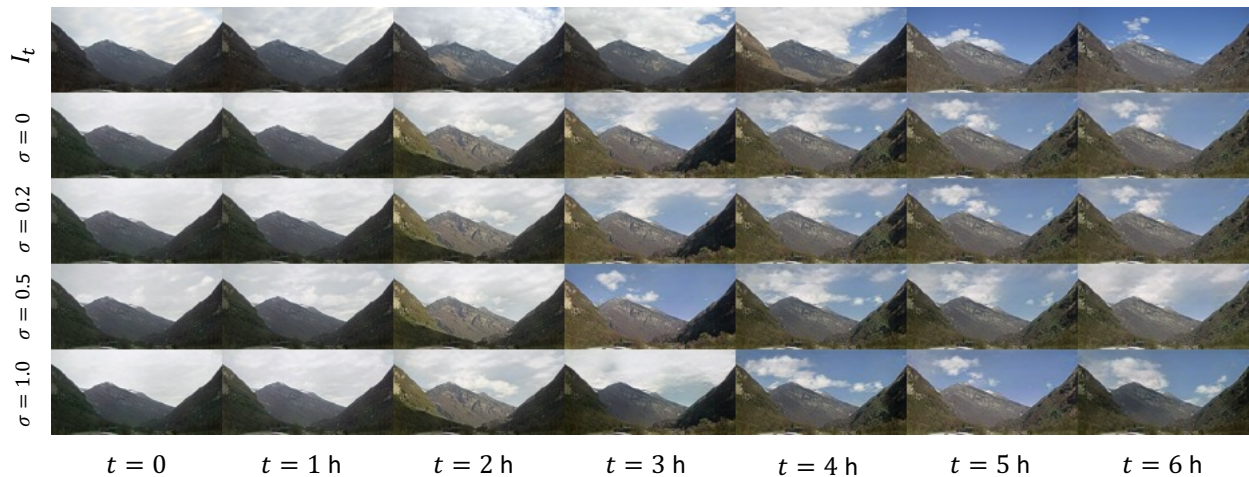


Figure 14: The effect of the noise variance on the diversity of visualizations synthesized by the generator. Increasing σ when sampling $z \sim \mathcal{N}(0, \sigma^2)$ leads to a greater diversity of images that are deemed consistent with the weather forecast. But note that the realised diversity is also a function of t : it is smallest at $t = 0$, and greatest when there is a change of weather conditions at $t = 3h$. *Top row*: A sequence of images taken by the Cevio camera between 6:00 and 12:00 UTC on March 16th, 2020. *Following rows*: Nowcasting visualizations generated with $\sigma = (0, 0.2, 0.5, 1.0)$.

5 Conclusions and Future Work

We have shown that photographic images can not only visualize the weather conditions of the past and the present, but can be useful for weather forecasts as well. Using conditional Generative Adversarial Networks, it is possible to synthesize photographic visualizations that look realistic, match the predicted weather conditions, transition seamlessly from observation to forecast, and show a high degree of visual continuity between consecutive forecasting lead times.

Meteorological services could use such visualizations to communicate their localized forecasts in an additional format that is immediately accessible to the user. They could also provide a service to communities and tourism organizations for creating forecast visualizations that are specific for their web camera feeds.

The visualization method introduced in this paper is mature enough to become the first generation of an operational forecast product. But there are several next steps which could improve its visual fidelity and accuracy.

Training GANs is computationally intensive, which is why we had to limit the image size to 64 by 128 pixels. But there exist techniques in the literature [e.g. Karras et al., 2018] that scale GANs to image sizes of at least a megapixel. Training the production grade high-resolution network could be done in the cloud on sufficiently capable hardware.

Our results of Sec. 4.2 indicate that the generator is rarely to blame for mismatches between the actual and the visualized conditions. Errors occur instead if the weather descriptor fails to accurately capture the conditions visible in the image. Using sub-hourly and sub-kilometer forecasts could improve the accuracy of the weather descriptors, and therefore the accuracy of the visualization method. Evaluating the forecast output fields at multiple locations in the line of sight of the camera could also be beneficial.

While the temporal evolution of the ground and illumination conditions looks natural, our GAN architecture still struggles with synthesizing the movement of the sun and isolated clouds across the sky.

We will continue to investigate non-local network layers that could complement the convolution layers. We will also investigate whether synthesizing whole sequences of images (instead of single images) can further improve the temporal evolution of nowcast visualizations.

Finally, if it is possible to quickly adapt a view-independent generator to a specific view (ideally with a single image), novel interactive applications of photographic visualizations would also become possible. Smartphone users could obtain personalized forecasts by taking an image of the local scenery and a reading of their geographic coordinates, and obtain a photographic animation that shows the predicted weather conditions in their near future.

Acknowledgments

We thank Rega for giving us the permission to use images from the Cevio camera in this study.

We thank Tanja Weusthoff for the preparation of the COSMO-1 forecast data.

We thank Christian Allemann, Yannick Bernard, Eliane Thürig, Deborah van Geijtenbeek and Abbès Zerdouk for evaluating the realism of individual generated images.

We thank Daniele Nerini for providing his expertise on nowcasting and post-processing of forecasts.

Code and Data Availability

A Tensorflow implementation of the generator and discriminator networks, as well as the code to reproduce the experiments presented in Sec. 4, is available in the companion repository.

The repository also contains the trained networks for the three camera locations, and additional generated images (of which Figures 8 to 14 are examples). The data used in the expert evaluations and their detailed results (summarized in Tables 2 and 3) are also available there.

The complete image archive and COSMO-1 data used for the training and evaluation of the networks

cannot be published online due to licensing restrictions. But it can be obtained free of charge for academic research purposes by contacting the MeetoSwiss customer service desk.

References

- Andrew Brock, Jeff Donahue, and Karen Simonyan. Large Scale GAN Training for High Fidelity Natural Image Synthesis. *arXiv:1809.11096 [cs, stat]*, February 2019.
- Ian Goodfellow, Jean Pouget-Abadie, Mehdi Mirza, Bing Xu, David Warde-Farley, Sherjil Ozair, Aaron Courville, and Yoshua Bengio. Generative adversarial nets. *Advances in neural information processing systems*, 27:2672–2680, 2014.
- Kaiming He, Xiangyu Zhang, Shaoqing Ren, and Jian Sun. Deep Residual Learning for Image Recognition. *arXiv:1512.03385 [cs]*, December 2015.
- Martin Heusel, Hubert Ramsauer, Thomas Unterthiner, Bernhard Nessler, and Sepp Hochreiter. GANs trained by a two time-scale update rule converge to a local nash equilibrium. In *Proceedings of the 31st International Conference on Neural Information Processing Systems, NIPS’17*, pages 6629–6640, Red Hook, NY, USA, December 2017. Curran Associates Inc. ISBN 978-1-5108-6096-4.
- Geoffrey Hinton, Nitish Srivastava, and Kevin Swersky. Neural networks for machine learning lecture 6a overview of mini-batch gradient descent. *Cited on*, 14(8):2, 2012.
- Sergey Ioffe and Christian Szegedy. Batch Normalization: Accelerating Deep Network Training by Reducing Internal Covariate Shift. *arXiv:1502.03167 [cs]*, March 2015.
- Phillip Isola, Jun-Yan Zhu, Tinghui Zhou, and Alexei A. Efros. Image-to-image translation with conditional adversarial networks. In *Proceedings of the IEEE Conference on Computer Vision and Pattern Recognition*, pages 1125–1134, 2017.
- Tero Karras, Timo Aila, Samuli Laine, and Jaakko Lehtinen. Progressive Growing of GANs for Improved Quality, Stability, and Variation. *arXiv:1710.10196 [cs, stat]*, February 2018.
- Diederik P. Kingma and Jimmy Ba. Adam: A Method for Stochastic Optimization. *arXiv:1412.6980 [cs]*, January 2017.
- Mehdi Mirza and Simon Osindero. Conditional Generative Adversarial Nets. *arXiv:1411.1784 [cs, stat]*, November 2014.
- Takeru Miyato, Toshiki Kataoka, Masanori Koyama, and Yuichi Yoshida. Spectral Normalization for Generative Adversarial Networks. *arXiv:1802.05957 [cs, stat]*, February 2018.
- Olof Mogren. C-RNN-GAN: Continuous recurrent neural networks with adversarial training. *arXiv:1611.09904 [cs]*, November 2016.
- Augustus Odena, Vincent Dumoulin, and Chris Olah. Deconvolution and checkerboard artifacts. *Distill*, 2016. doi: 10.23915/distill.00003.
- Alec Radford, Luke Metz, and Soumith Chintala. Unsupervised Representation Learning with Deep Convolutional Generative Adversarial Networks. *arXiv:1511.06434 [cs]*, January 2016.
- Olaf Ronneberger, Philipp Fischer, and Thomas Brox. U-Net: Convolutional Networks for Biomedical Image Segmentation. In Nassir Navab, Joachim Hornegger, William M. Wells, and Alejandro F. Frangi, editors, *Medical Image Computing and Computer-Assisted Intervention – MICCAI 2015*, Lecture Notes in Computer Science, pages 234–241, Cham, 2015. Springer International Publishing. ISBN 978-3-319-24574-4. doi: 10.1007/978-3-319-24574-4_28.
- U. Schättler, G. Doms, and C. Schraff. COSMO-Model Version 6.00: A Description of the Non-hydrostatic Regional COSMO-Model - Part VI: Model Output and Data Formats for I/O. 2021. doi: 10.5676/DWD_PUB/NWV/COSMO-DOC_6.00_VI.

- Edgar Schonfeld, Bernt Schiele, and Anna Khoreva. A U-Net Based Discriminator for Generative Adversarial Networks. In *2020 IEEE/CVF Conference on Computer Vision and Pattern Recognition (CVPR)*, pages 8204–8213, Seattle, WA, USA, June 2020. IEEE. ISBN 978-1-72817-168-5. doi: 10.1109/CVPR42600.2020.00823.
- Sifan Wu, Xi Xiao, Qianggang Ding, Peilin Zhao, Ying Wei, and Junzhou Huang. Adversarial sparse transformer for time series forecasting. *Advances in Neural Information Processing Systems*, 33, 2020.
- Jiahui Yu, Zhe Lin, Jimei Yang, Xiaohui Shen, Xin Lu, and Thomas S Huang. Generative image inpainting with contextual attention. In *Proceedings of the IEEE Conference on Computer Vision and Pattern Recognition*, pages 5505–5514, 2018.
- Sangdoon Yun, Dongyoon Han, Seong Joon Oh, Sanghyuk Chun, Junsuk Choe, and Youngjoon Yoo. CutMix: Regularization Strategy to Train Strong Classifiers with Localizable Features. *arXiv:1905.04899 [cs]*, August 2019.
- Han Zhang, Ian Goodfellow, Dimitris Metaxas, and Augustus Odena. Self-Attention Generative Adversarial Networks. *arXiv:1805.08318 [cs, stat]*, June 2019.